INTERNATIONAL JOURNAL FOR NUMERICAL METHODS IN FLUIDS
Int. J. Numer. Meth. Fluids 2005; **49**:149–170

Finite element modelling of free-surface flows with non-hydrostatic pressure and *k*–ε turbulence model

C. Leupi[1,*,†] and M. S. Altinakar[2,‡]

[1]*ISE-STI-LIN, Ecole Polytechnique Fédérale, Lausanne 1015, Switzerland*
[2]*NCCHE, The University of Mississipi, Carrier Hall Room 102 University, MS 38677, U.S.A.*

SUMMARY

Validation of 3D finite element model for free-surface flow is conducted using a high quality and high spatial resolution data set. The commonly numerical models with the conventional hydrostatic pressure still remain the most widely used approach for the solution of practical engineering problems. However, when a 3D description of the velocity field is required, it is useful to resort to a more accurate model in which the hydrostatic assumption is removed. The present research finds its motivation in the increasing need for efficient management of geophysical flows such as estuaries (multiphase fluid flow) or natural rivers with the presence of short waves and/or strong bathymetry gradient, and/or strong channel curvature. A numerical solution is based on the unsteady Reynolds-averaged Navier–Stokes equations on the unstructured grid. The eddy viscosity is calculated from the efficient *k*–ε turbulence model. The model uses implicit fractional step time stepping, and the characteristics method is used to compute the convection terms in the multi-layers system (suitable for the vertical stratified fluid flow), in which the vertical grid is located at predefined heights and the number of elements in the water column depends on water depth. The bottommost and topmost elements of variable height allow a faithful representation of the bed and the time-varying free-surface, respectively. The model is applied to the 3D open channel flows of various complexity, for which experimental data are available for comparison. Computations with and without non-hydrostatic are compared for the same trench to test the validity of the conventional hydrostatic pressure assumption. Good agreement is found between numerical computations and experiments. Copyright © 2005 John Wiley & Sons, Ltd.

KEY WORDS: validation; 3D finite element model; characteristics method; non-hydrostatic pressure; efficient *k*–ε turbulence model; multi-layers system; 3D open channel flows; unstructured grid

---

[*] Correspondence to: Celestin Leupi, ISE-STI-LIN, Ecole Polytechnique Fédérale, Lausanne 1015, Switzerland.
[†] E-mail: celestin.leupi@epfl.ch
[‡] E-mail: altinakar@ncche.olemiss.edu

Contract/grant sponsor: Swiss National Science Foundation; contract/grant number: 21-65095.01

Received 22 December 2004
Revised 25 March 2005
Accepted 29 March 2005

1. INTRODUCTION

The simulation of free-surface flows is widely applied for many problems such as the description of hydrodynamic currents, the transport of pollutants, for weather prediction, just to mention few. Several numerical models with the conventional hydrostatic pressure have been successfully applied for most of geophysical free-surface flows modelling. However, in the presence of short waves and/or strong bathymetry gradient, and/or strong channel curvature, a 3D description of the velocity field is required. Therefore it is useful to resort to a more accurate model in which the hydrostatic assumption is removed.

Many 3D non-hydrostatic models have been carried out with the aim to simulate open channel flows. Johns [1] showed a method for 2D vertical-plane problems without directly solving the vertical momentum equation, but determined vertical velocity from local continuity and non-hydrostatic pressure from the integrated vertical momentum equation. The approach would appear to be limited to steady problems. Nevertheless, the importance of non-hydrostatic pressure in sand-wave problems was demonstrated. Casulli and Stelling [2] incorporated non-hydrostatic pressure in the Cartesian scheme of Casulli and Cheng [3]. This showed some promising results but the influence of non-hydrostatic pressure on free-surface elevation was not included. Stansby and Zhou [4] using finite volume formulation, included non-hydrostatic pressure in momentum equations for incorporation in the surface elevation solution. At each time step the pressure and velocities were adjusted through the solution of Poisson equation. Promising results were shown, but this adjustment can influence the accuracy of the solution and the test were applied only to the 2D problems. The curved open channel flows are of more importance for environmental hydraulic engineering, and several researchers have been working on their numerical modelling. In such flows, the secondary flows generated by the channel curvature and the related background turbulence effects, need to be well understood. Lai *et al.* [5] have used finite volume method on the unstructured grid to simulate 3D flow in meandering channel. Wu *et al.* [6] and Olsen [7] used 3D numerical models to study the flow structure and mass transport in curved open channel. Chao *et al.* [8] have simulated the 3D unsteady curved open channel with standard k–ε turbulence model and the non-hydrostatic pressure on the conformal mesh. Most of these 3D models employed the rigid-lid approximation and/or conformal mesh for the free-surface treatment, which can poorly perform, especially in the presence of the strong curvature and/or strong bathymetry gradient (see Reference [9]).

The present model is based on the novel approach developed by Leupi *et al.* [10], in which the conservative formulation of the RANS is adopted as well as the multi-layers system (more suitable for the stratified fluid flow modelling) to provide an accurate resolution of the scheme.

The present work aims at validating 3D finite element solver model against well-known flows with the increasing difficulties, using a high quality and high spatial resolution data set.

In this study, the full 3D Reynolds-averaged Navier–Stokes (RANS) equations are solved using implicit time marching scheme, while discretization is conducted using Euler or Runge–Kutta scheme to obtain a set of algebraic equations. The horizontal grid is built on the xy plane unstructured triangular grid. The vertical grid is located at predefined heights and the number of elements in the water column depends on water depth (the number of active (wetted) layer is defined at each time step, and the vertical grid is regenerated at each time step). The bottommost and topmost elements of variable height allow a faithful representation of the bed and the time-varying free-surface, respectively. The model offers the capability of using either hydrostatic or hydrodynamic pressure distribution, and the model uses an efficient fractional time-step scheme of Mohammadi and Pironneau [11] for the state-of-art k–ε turbulence closure.

An outline of this paper is as follows: In Section 2, we review the governing equations, the associated boundary conditions and we derive a weak formulation suitable for the 3D model. In Section 3, we introduce the discretization of the physical domain, the finite element approximation and the space–time discretization. In Section 4 we propose some numerical tests of various complexity with the aim of outlining the good properties of the model.

2. MATHEMATICAL MODELS FOR TURBULENT FREE-SURFACE FLOWS

A brief description of the hydrostatic version with the turbulent model is provided in Reference [10]. Let us consider an incompressible fluid body in a 3D time-varying domain $\widehat{\Omega}$ in Figure 1. Let Ω the projection of $\widehat{\Omega}$ on the xy horizontal plane, bounded by the free-surface Γ_s given by $z=\eta(x,y,t)$, the bottom topography Γ_b given by $z=-\mathfrak{h}(x,y)$, the open boundary denoted by Γ_o. Where $\mathfrak{h}(x,y)$ is the distance between the bottom and the reference plane xy and $\eta(x,y,t)$ the elevation of the free-surface with the respect to the reference plane xy.

For description of the turbulent motion, the pressure p can be written as the sum of an hydrostatic term p_h and an hydrodynamic correction $p_{nh}=\rho\tilde{p}$,

$$p(\mathbf{x},t)=p_h+p_{nh}=p_a+g\rho_0(\eta-z)+g\int_z^{\eta}\Delta\rho\,\mathrm{d}z+\rho\tilde{p}(\mathbf{x},t) \tag{1}$$

The 3D non-hydrostatic RANS equations reads

$$\nabla_H\cdot\mathbf{U}+\frac{\partial w}{\partial z}=0 \tag{2}$$

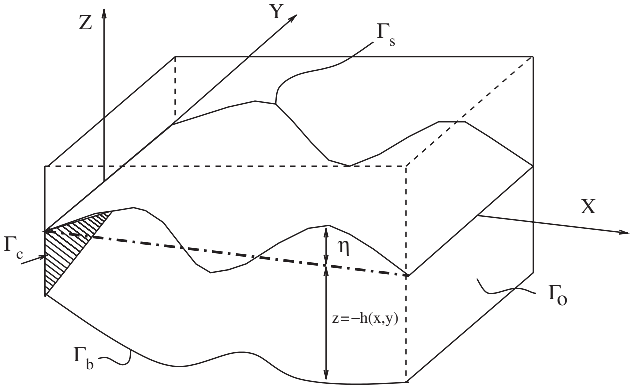

Figure 1. Physical domain and its representation.

$$\frac{D\mathbf{U}}{Dt} + g\nabla_H \eta - \nabla_H(v_T \nabla_H \mathbf{U}) - \frac{\partial}{\partial z}\left(v_T \frac{\partial \mathbf{U}}{\partial z}\right) + g\nabla\left(\int_{\mathfrak{h}}^{\eta} \frac{\Delta\rho}{\rho_0}\,\mathrm{d}z\right) + \frac{1}{\rho_0}\nabla \tilde{p} = \mathbf{F}_{xy} \tag{3}$$

$$\frac{Dw}{Dt} - \nabla_H(v_T \nabla_H w) - \frac{\partial}{\partial z}\left(v_T \frac{\partial w}{\partial z}\right) + \frac{1}{\rho_0}\frac{\partial \tilde{p}}{\partial z} = 0 \tag{4}$$

$$\frac{\partial \eta}{\partial t} + \nabla_H \cdot \int_{-\mathfrak{h}}^{\eta} \mathbf{U}\,\mathrm{d}z = 0 \tag{5}$$

where $\mathbf{U} = (u, v)^{\mathrm{T}}$ is the horizontal velocity vector, $\mathbf{F}_{xy} = (fv, -fu)^{\mathrm{T}}$ is vector of body forces with f the Coriolis parameter, g is the gravitational acceleration, v_T is the eddy viscosity, (see Reference [12]). $\nabla\cdot$ is the 3D divergence operator, D/Dt represents the material derivative, and $\nabla_H\cdot$ is the surface divergence operator. ρ, ρ_0 are, respectively, the fluid density and the basic water density.

In Equation (3), the vertical eddy viscosity is defined as

$$v_T = v + c_\mu \frac{k^2}{\varepsilon} \tag{6}$$

in which v is the kinematic viscosity.

The quantities k and ε are described by a generic form of equations [11].

$$\frac{Dk}{Dt} - \nabla \cdot \left[c_\mu \frac{k^2}{\varepsilon} \nabla k\right] = c_\mu \frac{k^2}{\varepsilon} G - \varepsilon \tag{7}$$

$$\frac{D\varepsilon}{Dt} - \nabla \cdot \left[c_\varepsilon \frac{k^2}{\varepsilon} \nabla \varepsilon\right] = \frac{c_1}{2} kG - c_2 \frac{\varepsilon^2}{k} \tag{8}$$

The values of the turbulent constants are: $c_1 = 0.126$, $c_2 = 0.07$, $c_\mu = 0.09$, $c_\varepsilon = 1.92$. The production term is represented by the squared shear frequency, G, (see Reference [13]), such as:

$$G = \tfrac{1}{2}(\|\nabla \mathbf{V}\| + \|\nabla \mathbf{V}\|^{\mathrm{T}})^2 \tag{9}$$

where $\|.\|$ represents the Euclidian norm, $\mathbf{V} = \mathbf{V}(u, v, w)$ is the 3D velocity vector.

2.1. Boundary and initial conditions

At the bottom, the no-slip condition is applied together with a zero normal velocity component to Γ_{b}. This second condition can be represented by

$$w_{\mathrm{b}} = u_{\mathrm{b}} \frac{\partial h}{\partial x} + v_{\mathrm{b}} \frac{\partial h}{\partial y} = 0 \quad \text{on } \Gamma_{\mathrm{b}} \tag{10}$$

The equilibrium assumption is adopted at the bed (i.e. local balance between production of turbulent kinetic energy and the rate of dissipation). The wall functions are applied to relate the velocity to the bed shear velocity u_* in the rough turbulent boundary layer, i.e. at the distance, δ_n, normal to the nearest wall such that, $30v/u_* < \delta_n < 100v/u_*$ (see References [6, 10, 14, 15]).

At free-surface Γ_s, the kinematic condition states that the fluid particles at the free-surface move with the free-surface, one can find,

$$w_s = \frac{\partial \eta}{\partial t} + u_s \frac{\partial \eta}{\partial x} + v_s \frac{\partial \eta}{\partial y} \quad \text{on } \Gamma_s \tag{11}$$

The *depth-integrated continuity equation* (5) is obtained from the integration of the (local) continuity equation (2) in the z direction using the suitable the kinematic free-surface and bottom boundary conditions.

At the free-surface, without wind stress, the boundary conditions for turbulent quantities (see Reference [4]) read

$$\frac{\partial k}{\partial z} = 0; \quad \varepsilon = \frac{(kc_\mu)^{1.5}}{0.07\kappa h} \tag{12}$$

where $c_\mu = 0.09$ is a model constant.

At the open outlet boundary denoted by Γ_o, the Neumann boundary conditions are applied for the velocity ($\partial \mathbf{U}/\partial n = 0$), and other variables (i.e. a zero normal gradient through these surfaces), where $\partial/\partial n$ is a normal derivative to the surface. At the vertical wall Γ_c, the slip boundary conditions are used by setting all normal components to the vertical wall equal to zero ($\mathbf{U}_n = 0$), and Neumann boundary conditions are applied for turbulent quantities.

3. FINITE ELEMENT APPROXIMATION

In this section we introduce the weak formulation and its space–time discretization. The physical 3D domain (Figure 2) is embedded in a parallelepiped composed of $\mathcal{N}$ layers. The horizontal projection of the domain Ω is discretized using an unstructured triangular mesh $\mathcal{T}_h$. The same mesh is placed (fixed) in the middle of each layer. The vertical grid is located at predefined heights and the number of elements in the water column depends on water depth (the number of active or wetted layers is defined at each time step, and the vertical grid is regenerated at each time step). The bottommost and topmost elements of variable height allow a faithful representation of the bed and the time-varying free-surface, respectively. In a layer, each triangular mesh element defines a 3D prismatic element. The horizontal components of the velocity vector are defined at the middle of edges of the triangular mesh elements, while the vertical components are associated with the lower and upper horizontal faces of the element.

The horizontal velocity is approximated combining the lowest order Raviart–Thomas element ($\mathbb{RT}_0$) in xy plane with the $\mathbb{P}_1$ elements along the vertical direction. For every integer $r \geqslant 0$ we denote by $\mathbb{P}_r(T)$ the space of polynomials of degree $\leqslant r$ on each triangle $T \in \mathcal{T}_h$ (see Figure 2) and consider the Raviart–Thomas vector finite element space of lowest order $\mathbb{RT}_0$ (see References [10, 16, 17]), with the following functional spaces $H_{0,c}(\text{div};\Omega) = \{\tau : \tau \in (L^2(\Omega))^2, \text{div}\tau \in L^2(\Omega), \tau \cdot \mathbf{n} = 0 \text{ on } \Gamma_c\}$, Γ_c denotes the vertical solid wall; The anisotropic Sobolev space $H^1(\Omega)\{\psi \in L^2(\Omega) : \partial_{x_i}\psi \in L^2(\Omega),\ i = 1,\ldots,\mathrm{d}\}$ and the following finite

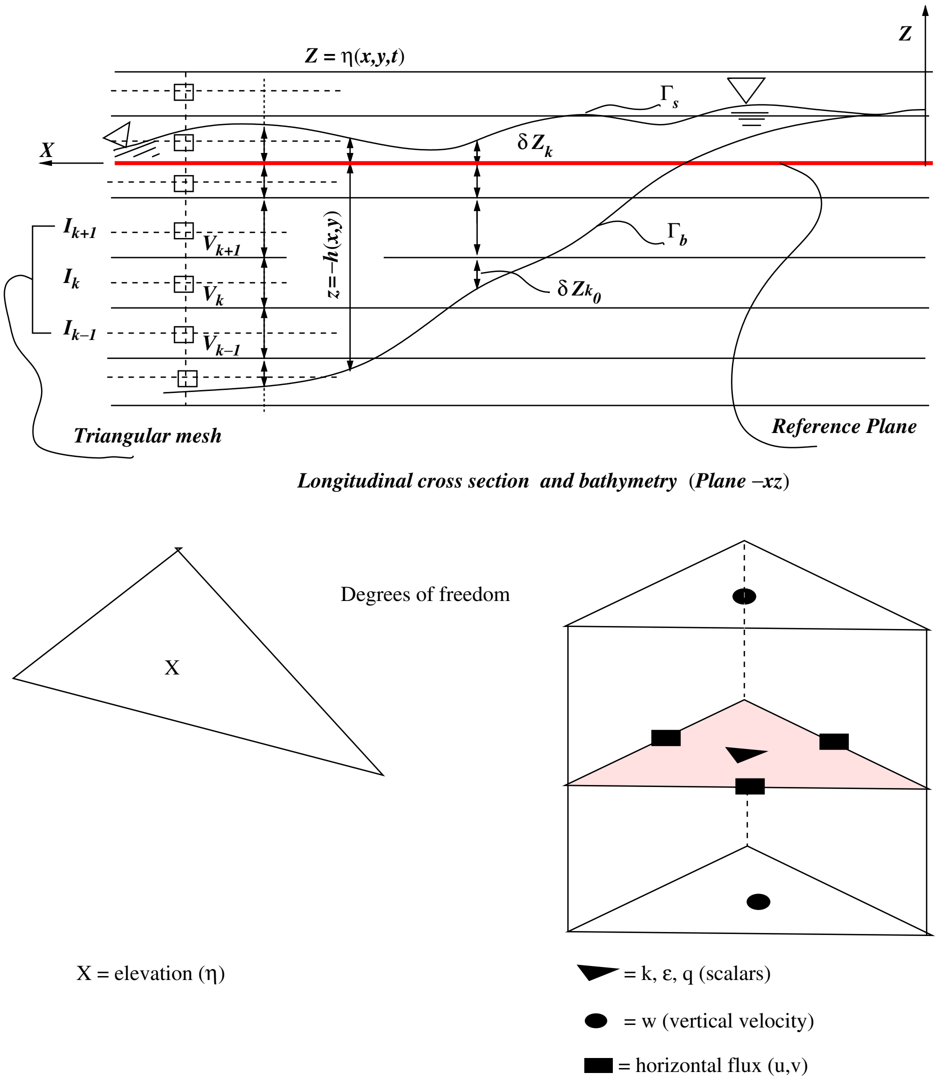

Longitudinal cross section and bathymetry (Plane –xz)

Figure 2. Physical domain representation with numerical variables location.

element spaces:

$$\begin{aligned} \mathbb{Q}_h &= \{\mathbf{q}\in H_{0,c}(\mathrm{div};\Omega) \mid \mathbf{q}|_T \in \mathbb{RT}_0(T)\ \forall T\in\mathcal{T}_h\}\\ U_h &= \{\psi\in L^2(\Omega)\mid \psi|_T\in\mathbb{P}_0(T)\ \forall T\in\mathcal{T}_h\}\\ W_{I^1_{1/2}} &= \{\varphi\in \mathrm{C}^0([-\mathfrak{h},\eta])\mid \varphi|_{I_{k+1/2}}\in\mathbb{P}_1(I_{k+1/2})\ \forall I_{k+1/2}\in\mathcal{I}_{1/2}\}\\ W_{I^1_1} &= \{\zeta\in \mathrm{C}^0([-\mathfrak{h},\eta])\mid \zeta|_{I_k}\in\mathbb{P}_1(I_k) \text{ with } \zeta|_{-\mathfrak{h}}=0 \text{ and } \zeta|_\eta=0\ \forall I_k\in\mathcal{I}_1\}\\ W_{I^0_1} &= \{\chi\in L^2(\Omega)\mid\chi|_k\in\mathbb{P}_0(p)\ \forall I_k\in\mathcal{I}_1\} \end{aligned} \tag{13}$$

The approximation solutions for the variables read as

$$
\begin{aligned}
\mathbf{U}_h^{n+1}(\mathbf{x},z) &= \sum_{k=k_0}^{\mathscr{K}} \sum_{l=1}^{N_{ed}} \jmath^{n+1} \tau_l(\mathbf{x}) \varphi_k(z) \quad \forall \tau \in \mathbb{Q}_h \ \ \forall \varphi \in W_{\mathscr{I}^1_{1/2}} \\
\eta_h^{n+1}(\mathbf{x}) &= \sum_{j=1}^{N_{el}} \eta_j^{n+1} \psi_j(\mathbf{x},z) \quad \forall \psi \in U_h \\
w_h^{n+1}(\mathbf{x},z) &= \sum_{s=1}^{N_{el}} \sum_{k=k_0}^{\mathscr{K}-1} w_{s,h}^{n+1} \psi_s(\mathbf{x}) \zeta_{k+1/2}(z) \quad \forall \psi \in U_h \ \ \forall \zeta \in W_{\mathscr{I}^1_1} \\
\tilde{p}_h^{n+1}(\mathbf{x},z) &= \sum_{s=1}^{N_{el}} \sum_{k=k_0}^{\mathscr{K}-1} \tilde{p}_{s,h}^{n+1} \psi_s(\mathbf{x}) \chi_k(z) \quad \forall \psi \in U_h \ \ \forall \chi \in W_{\mathscr{I}^0_1} \\
k_h^{n+1}(\mathbf{x},z) &= \sum_{s=1}^{N_{el}} \sum_{k=k_0}^{\mathscr{K}-1} k_{s,h}^{n+1} \psi_s(\mathbf{x}) \chi_k(z) \quad \forall \psi \in U_h \ \ \forall \chi \in W_{\mathscr{I}^0_1} \\
\varepsilon_h^{n+1}(\mathbf{x},z) &= \sum_{s=1}^{N_{el}} \sum_{k=k_0}^{\mathscr{K}-1} \varepsilon_{s,h}^{n+1} \psi_s(\mathbf{x}) \chi_k(z) \quad \forall \psi \in U_h \ \ \forall \chi \in W_{\mathscr{I}^0_1}
\end{aligned}
\tag{14}
$$

with $\jmath_{l,k} = \int_{el} \mathbf{U}_k \cdot \mathbf{n}_l \, \mathrm{d}\sigma, l = 1, \ldots, N_{ed}$.

N_{ed} and N_e denote, respectively, the number of (oriented) edges e_l and triangles T_j in the mesh, by k_0 and $\mathscr{K}$), respectively, the indice of bottom and uppermost layer, N_p is the total number of active prisms.

To approximate the system of Equations (2), (5), (3) on each prism (p), using Greens formula and the boundary conditions the problem statement is to find $\mathbf{U} \in Q_h \times W_{I^1_{1/2}}$, $w \in U_h \times W_{I^1_1}$, $p_r \in U_h \times W_{I^0_1}$, $k \in U_h \times W_{I^0_1}$, $\varepsilon \in U_h \times W_{I^0_1}$, such that:

$$
\int_{\partial p} w^{n+1} n_z \, \mathrm{d}s = \int_{\partial p} \mathbf{U}^{n+1} \cdot \mathbf{n}_{xy} \, \mathrm{d}S \quad \forall p \tag{15}
$$

$$
\int_\Omega \frac{\eta^{n+1} - \eta^n}{\Delta t} \psi \, \mathrm{d}\Omega + \int_\Omega \left(\nabla_H \cdot \int_{-\mathfrak{h}}^{\eta^n} \mathbf{U}^{n+1} \, \mathrm{d}z \right) \psi \, \mathrm{d}\Omega = 0 \tag{16}
$$

$$
\begin{aligned}
&\int_\Omega \psi \int_{-\mathfrak{h}}^{\eta^n} \frac{w^{n+1} - w(\mathbf{X}^n)}{\Delta t} \zeta \, \mathrm{d}z \, \mathrm{d}\Omega - \int_{\partial\Omega} \int_{-\mathfrak{h}}^{\eta^n} v_T^n \left[\tau \nabla_H w^{n+1} + \frac{1}{2|T|} \right] \mathrm{d}\gamma \, \mathrm{d}z \\
&\quad - \frac{1}{\rho_0} \int_\Omega \psi \int_{-\mathfrak{h}}^{\eta^n} \frac{\partial}{\partial z} \left(v_T^n \frac{\partial w^{n+1}}{\partial z} \right) \zeta \, \mathrm{d}z + \int_\Omega \psi \int_{-\mathfrak{h}}^{\eta} \frac{\partial p_r^{n+1}}{\partial z} \chi \, \mathrm{d}z
\end{aligned}
\tag{17}
$$

$$
\begin{aligned}
\int_\Omega \int_{-\mathfrak{h}}^{\eta^n} \varphi \frac{\mathbf{U}^{n+1} - \mathbf{U}(\mathbf{X}^n)}{\Delta t} \cdot \tau \, \mathrm{d}z \, \mathrm{d}\Omega = g &\int_\Omega \int_{-\mathfrak{h}}^{\eta^n} \varphi \eta^{n+1} \nabla_H \cdot \tau \, \mathrm{d}z \, \mathrm{d}\Omega - \int_\Omega [u_\mathfrak{b}^{n+1} \cdot \tau \varphi |_\mathfrak{h}] \, \mathrm{d}\Omega \\
&- \int_{\partial\Omega} \int_{-\mathfrak{h}}^{\eta^n} v_T^n \left[\tau \nabla_H \upsilon^{n+1} + \frac{1}{2|T|} \right] \mathrm{d}\gamma \, \mathrm{d}z \\
&- v_v^n \int_\Omega \int_{-\mathfrak{h}}^{\eta^n} \tau \cdot \frac{\partial \mathbf{U}^{n+1}}{\partial z} \frac{\partial \varphi}{\partial z} \, \mathrm{d}z \, \mathrm{d}\Omega
\end{aligned}
$$

$$
\begin{aligned}
&+g\int_{\Omega}\varphi\nabla\left(\int_{\mathrm{h}}^{\eta^n}\frac{\rho^n-\rho_0}{\rho_0}\,\mathrm{d}z\right)\tau\,\mathrm{d}\Omega\\
&+\int_{\Omega}\int_{-\mathfrak{h}}^{\eta^n}\varphi\mathbf{f}^n_{xy}\cdot\tau\,\mathrm{d}z\,\mathrm{d}\Omega+\frac{1}{\rho_0}\int_{\Omega}\psi\int_{-\mathfrak{h}}^{\eta^n}\nabla p_r^{n+1}\chi\,\mathrm{d}\Omega\,\mathrm{d}z\\
&-g\int_{\Gamma_0\cap\Gamma_b}\int_{-\mathfrak{h}}^{\eta^n}\varphi\eta^{n+1}\tau\cdot\mathbf{n}\,\mathrm{d}z\,\mathrm{d}\gamma \qquad (18)
\end{aligned}
$$

$$
\begin{aligned}
\int_{\Omega}\int_{-\mathfrak{h}}^{\eta^n}\chi\frac{(k^{n+1}-k^n(\mathbf{X}))}{\Delta t}\psi\,\mathrm{d}\Omega\,\mathrm{d}z=&\int_{\partial\Omega}\int_{-\mathfrak{h}}^{\eta^n}\chi\nabla\cdot\left[c_\mu\frac{k^{n2}}{\varepsilon^n}\nabla k^{n+1}\right]\cdot\mathbf{n}\psi\,\mathrm{d}\Omega\,\mathrm{d}z\\
&+\int_{\Omega}\int_{-\mathfrak{h}}^{\eta^n}\chi\left(c_\mu\frac{(k^n)^2}{\varepsilon^n}G^n-\varepsilon^n\frac{k^{n+1}}{k^n}\right)\psi\,\mathrm{d}\Omega\,\mathrm{d}z \qquad (19)
\end{aligned}
$$

$$
\begin{aligned}
\int_{\Omega}\int_{-\mathfrak{h}}^{\eta^n}\chi\frac{(\varepsilon^{n+1}-\varepsilon^n(\mathbf{X}))}{\Delta t}\psi\,\mathrm{d}\Omega\,\mathrm{d}z=&\int_{\partial\Omega}\int_{-\mathfrak{h}}^{\eta^n}\chi\left[c_\mu\frac{k^{n2}}{\varepsilon^n}(\nabla\varepsilon^{n+1})\right]\cdot\mathbf{n}\psi\,\mathrm{d}\Omega\,\mathrm{d}z\\
&+\int_{\Omega}\int_{-\mathfrak{h}}^{\eta^n}\chi\left(\frac{c_1}{2}k^nG^n-c_2\frac{(\varepsilon^n\varepsilon^{n+1})}{k^n}\right)\psi\,\mathrm{d}\Omega\,\mathrm{d}z \qquad (20)
\end{aligned}
$$

where $|T|$ denotes the surface of the triangle. n_{xy}, n_z are, respectively, the horizontal and vertical components of the normal vector $\mathbf{n}$.

The Lagrange–Galerkin (or characteristic-Galerkin) approach is used (see References [11, 16]) to discretize the convection terms, while the Euler scheme or more accurate Runge–Kutta is used to obtain the algebraic system. At each time step it is only required to solve a set of the positive definite symmetric matrices for the fluxes using the conjugate gradient solver. To avoid spurious numerical oscillations, the source term, G, in the k equation has been discretized explicitly, while the sink term has been discretized using the quasi-implicit forms and consequently the nonlinear terms have been linearized (see References [11, 12]). The characteristics method used here can guarantee the positivity of k and ε (monotonicity of the solution). The model adopts the fractional time-step scheme from Mohammadi and Pironneau [10, 11], to solve turbulence equations. In this algorithm, the ordinary system of turbulence equations are splitted by first solving the convection step (containing only the terms of order zero) and the diffusion step (containing the other remaining terms) finally. Consequently, the positivity of k and ε is preserved as well as the stability of the scheme (see Reference [10]).

4. NUMERICAL RESULTS

To check the validity of the developed model, the computations were carried out against well-known flows with the increasing complexity, using a high quality and high spatial resolution data set. In the spatial discretization, the lowest layer thickness δZ_b is chosen such that, the adjacent grid point (first vertical grid point) should lie within the rough turbulent boundary layer, i.e. $30\nu/u_* < \delta_n = \delta Z_{\mathrm{b}}/2 < 100\nu/u_*$. In the wall region, the shear stress can be assumed constant, $u_* \approx 0.1U$, where U is a flow mean velocity (see Reference [18]), δ_n is a normal vertical distance of the first vertical mesh point from the bottom.

4.1. *The model accuracy*

To compute the decay of the homogeneous turbulence convected by a uniform flow, some analytical solutions have been used (see Reference [11]) for the steady open channel flow (see Reference [10, 19]):

$$k = k^0 \left(1 + (c_{\mathrm{a}} - 1)x\frac{\varepsilon^0}{k^0}\right)^{1/(1-c_{\mathrm{a}})} \tag{21}$$

$$\varepsilon = \varepsilon^0 \left(1 + (c_{\mathrm{a}} - 1)x\frac{\varepsilon^0}{k^0}\right)^{c_{\mathrm{a}}/(1-c_{\mathrm{a}})} \tag{22}$$

where x is the longitudinal coordinate, $c_{\mathrm{a}} = 2.06$ is a constant, k^0 and ε^0 are, respectively, the initial values of the turbulent kinetic energy and its rate of dissipation. In this computations, the channel is 38[m] long, the width is $B = 2$[m] and the flow depth is $h = 0.183$[m]. The discharge is $Q = 0.25$[m/s], the bed roughness is $k_{\mathrm{s}} = 0.0042$[m], and the bed slope is set to $S_0 = 0.000624$. Computations were conducted using 100 layers, with the lowest layer thickness $\delta Z_{\mathrm{b}} = 0.002$[m].

Figures 3 and 4 show the good agreement between computed and analytical solutions.

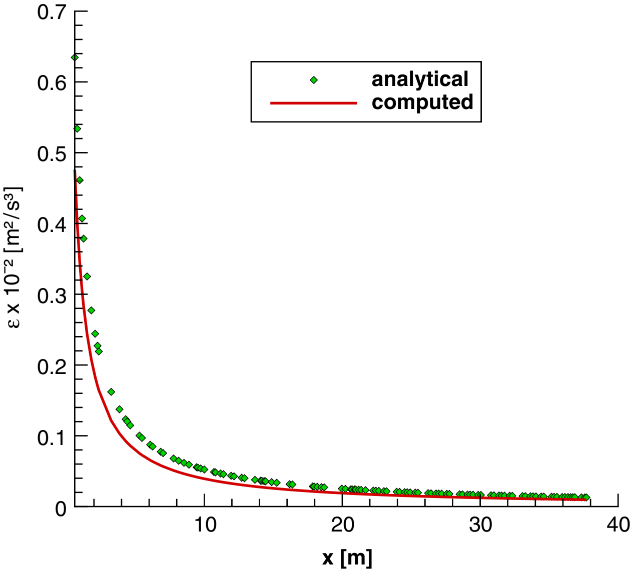

Figure 3. Computed ε versus analytical solution.

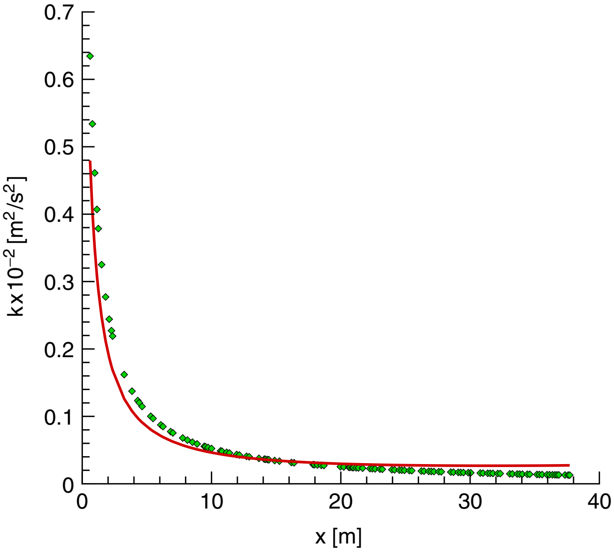

Figure 4. Computed k versus analytical solution.

4.2. *Space and time order accuracy*

In the following, the order spatial accuracy of the model is investigated through the above analytical solutions (for the temporal accuracy, we used the same Equations (21) and (22), in which x is replaced by t). One can determine the observed order of spatial accuracy on the space increment by calculating (see Reference [20]),

$$p(\Phi) = \log\left(\frac{\|\Phi_n - \Phi_{n+1}\|_2}{\|\Phi_{n+1} - \Phi_{n+2}\|_2}\right) \Big/ \log(2) \tag{23}$$

where $p(\Phi)$ denotes the observed order of spatial accuracy for the computed turbulence variable $\Phi = (k, \varepsilon)$ on different mesh sizes (denotes by n, $n+1$, $n+2$), and the differences are measured in the L_2-norm. The computations were performed on different sequences of mesh sizes (to determine the spatial order accuracy) and on different time-step sizes (to determine the temporal accuracy). The error between the exact solution Φ_e and analytical solutions $\Phi = (k, \varepsilon)$ is calculated using a high-order Gaussian quadrature formula to compute the following L_2-norm:

$$\|e\| = \|\Phi_e - \Phi\| = \left[\int_{\widehat{\Omega}} |\Phi_e - \Phi|^2 \, d\widehat{\Omega}\right]^{1/2} \tag{24}$$

Table I shows the observed order of spatial accuracy, where C_A represents a surface of the finest grid size (triangle) of the 2D-horizontal unstructured mesh. Figure 5(b) shows the expected spatial accuracy behaviour, i.e. second-order space accuracy, and indicates a convergence of the scheme for k and ε. Moreover, (ε equation behaves better) for a specific error tolerance, both solutions do not depend on the mesh size.

Table I. Spatial order accuracy.

$n(\Delta t=\sqrt{C_{\mathrm{A}}}[\mathrm{s}])$	$C_{\mathrm{A}}[\mathrm{m}^2]$	$k[\mathrm{m}^2/\mathrm{s}^2]$	$\varepsilon[\mathrm{m}^2/\mathrm{s}^3]$	$p(k)$	$p(\varepsilon)$
0	0.90537	0.09444869	0.0005053	1.7523201	1.1594802
1	0.45084	0.06473693	0.0007306	1.5348852	1.6964046
2	0.22551	0.04930999	0.0012773	1.8440260	1.8364252
3	0.11437	0.02277905	0.0027249	1.9016979	1.7976704
4	0.05586	0.01535665	0.0030808	1.9556649	1.9763579
5	0.02833	0.00823566	0.0033009	1.9997129	1.9980793
6	0.01406	0.00649211	0.0033198	2.0018692	2.0930549
7	0.00713	0.00648377	0.0033198	2.0018511	2.0919611

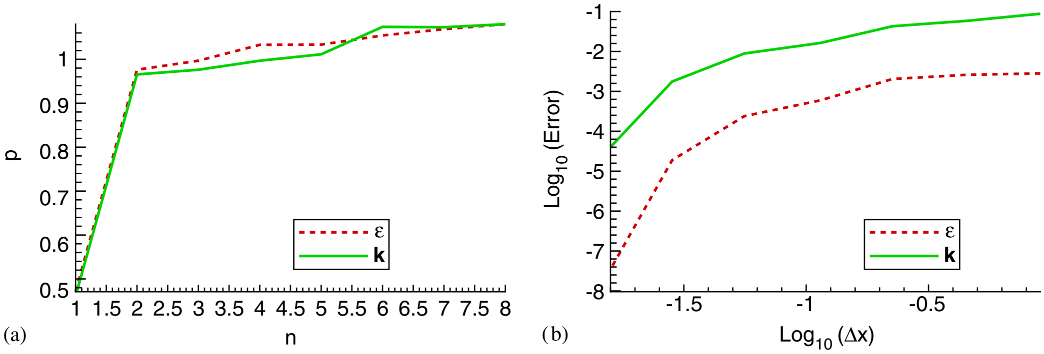

Figure 5. Space–time accuracy of the model: (a) observed order p of temporal accuracy versus different mesh sizes; and (b) observed order of spatial accuracy versus different time-step sizes.

Table II. Temporal order accuracy.

$n(\Delta t=\sqrt{C_{\mathrm{t}}}[\mathrm{s}])$	C_{t}	$k[\mathrm{m}^2/\mathrm{s}^2]$	$\varepsilon[\mathrm{m}^2/\mathrm{s}^3]$	$p(k)$	$p(\varepsilon)$
0	0.2	0.0098023	0.0004865	0.460602294	0.470819844
1	0.15	0.0018911	0.0012081	0.965543241	0.976251193
2	0.1	0.0257790	0.0021249	0.976235828	0.996778353
3	0.08	0.0394728	0.0029808	0.996763275	1.032926204
4	0.06	0.0583956	0.0031808	1.011424351	1.033425036
5	0.05	0.0643692	0.0033198	1.073921159	1.054290358
6	0.02	0.0647604	0.0033585	1.073049571	1.068591611
7	0.01	0.0648377	0.0033874	1.079972414	1.079981914

Table II shows the observed order of temporal accuracy, where C_{t} is a time-step constant. The time characteristic-Galerkin for the turbulence model uses first-order explicit backward Euler scheme to preserve the monotonicity of the scheme. The time discretization is therefore first-order accurate. Consequently, the coupled system can be at most first-order time accurate as confirmed in Figure 5, in which we use the finest mesh corresponding to the last line of Table II.

4.3. *Unsteady and non-uniform open channel flow*

The channel layout and dimensions as well as the given discharge hydrograph are shown in Figure 6. The channel is 18[m] long, the width is $B = 0.60$[m]. The rough bed has an equivalent roughness height, $k_s = 0.0058$[m]. The flow depth at the outflow (downstream end of the flume) is 0.13[m]. The experimental data are available for the flow case (see Reference [21]). The mean grid size is about $\Delta x = 0.08$[m] and the time step is set to

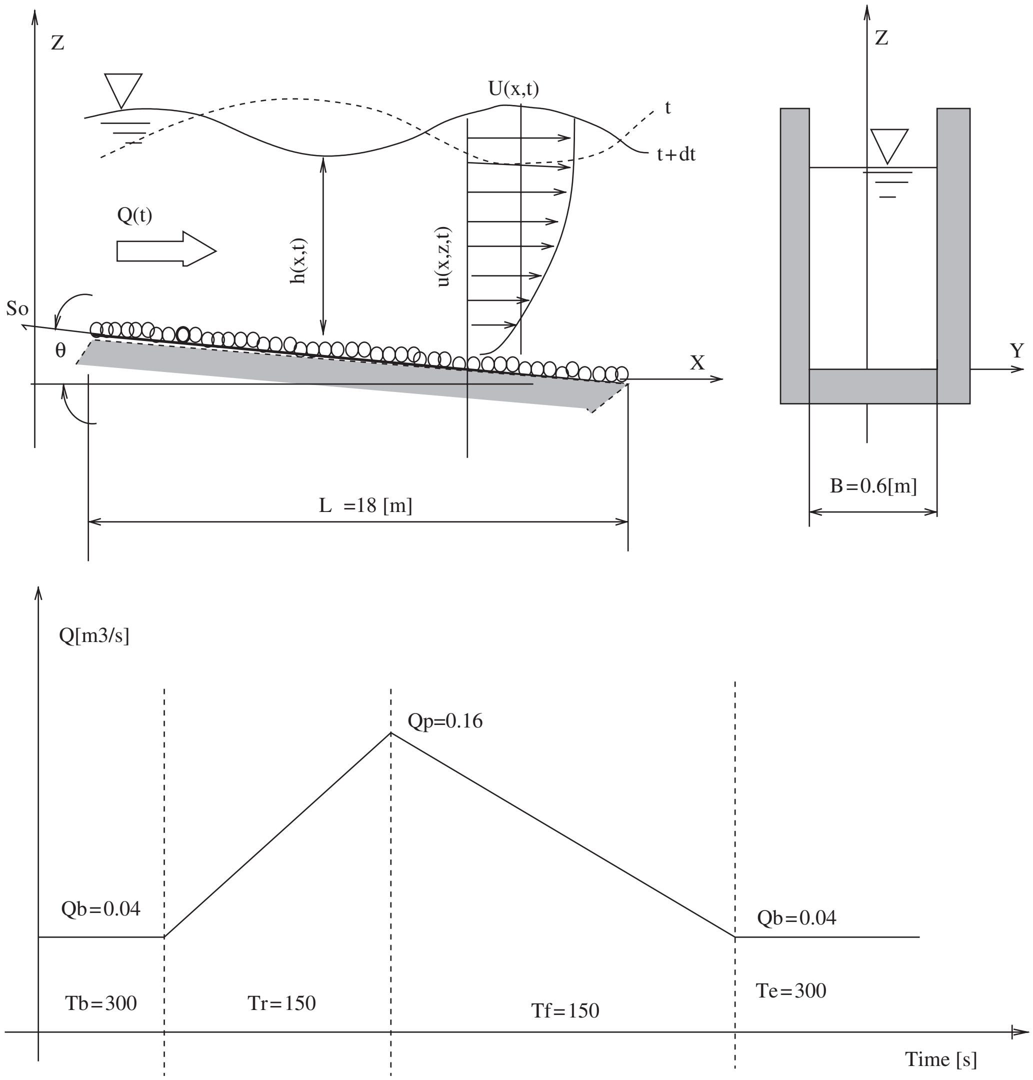

Triangular hydrograph

Figure 6. Unsteady open channel and triangular hydrograph.

$\Delta t = 0.1$[s]. Computations were conducted using 20 layers, with the lowest layer thickness $\delta Z_b = 0.002$[m]. The pictures in Figure 7 show flow depth time variation at the selected stations $x = 10.78$[m] and $x = 14.08$[m]. The model produces the surface ondulation as expected for the non-uniform flow, and good agreement is found between computations and experiments.

4.3.1. Error between computed depth and analytical solution. Error estimation is conducted between the computed flow depth (h_c) and experiments (h) at the selected sections $x = 10.78$ [m] and $x = 14.08$[m], using the following expression:

$$\text{Error}(h) = (h - h_c) \tag{25}$$

Figure 8 shows the flow depth values at time $T = 350$[s]. The error is found to be less than 0.0006[m], which is to confirm the good accuracy of the numerical model.

4.3.2. Computations versus experiments. Figure 9 shows the comparison between computed and measured distributions of the velocity, the eddy viscosity, and the shear stress at two stations $x = 10.78$[m] and $x = 14.08$[m] at time at $T = 700$ s. The computed velocity, eddy

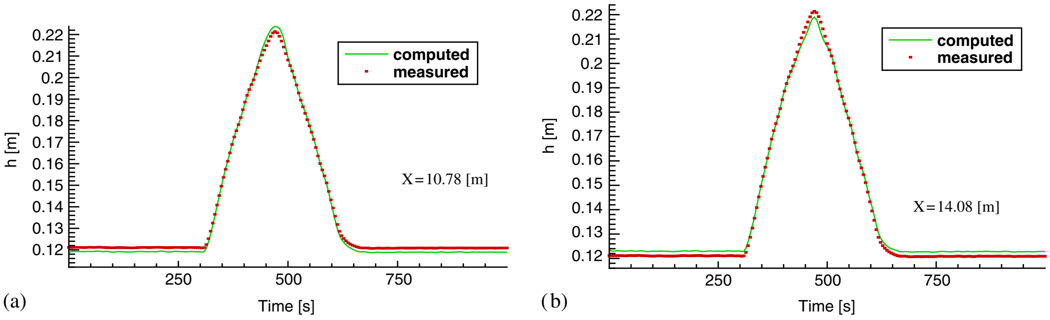

Figure 7. Computed flow depth versus experiments at the sections at the time $T = 350$[s]: (a) $x = 10.78$[m]; and (b) $x = 14.08$[m].

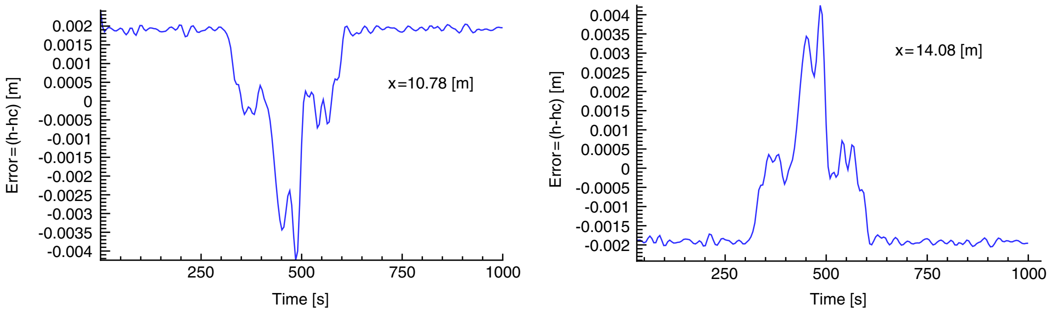

Figure 8. Error between computed flow depth and experiments at the selected sections at the time $T = 350$[s].

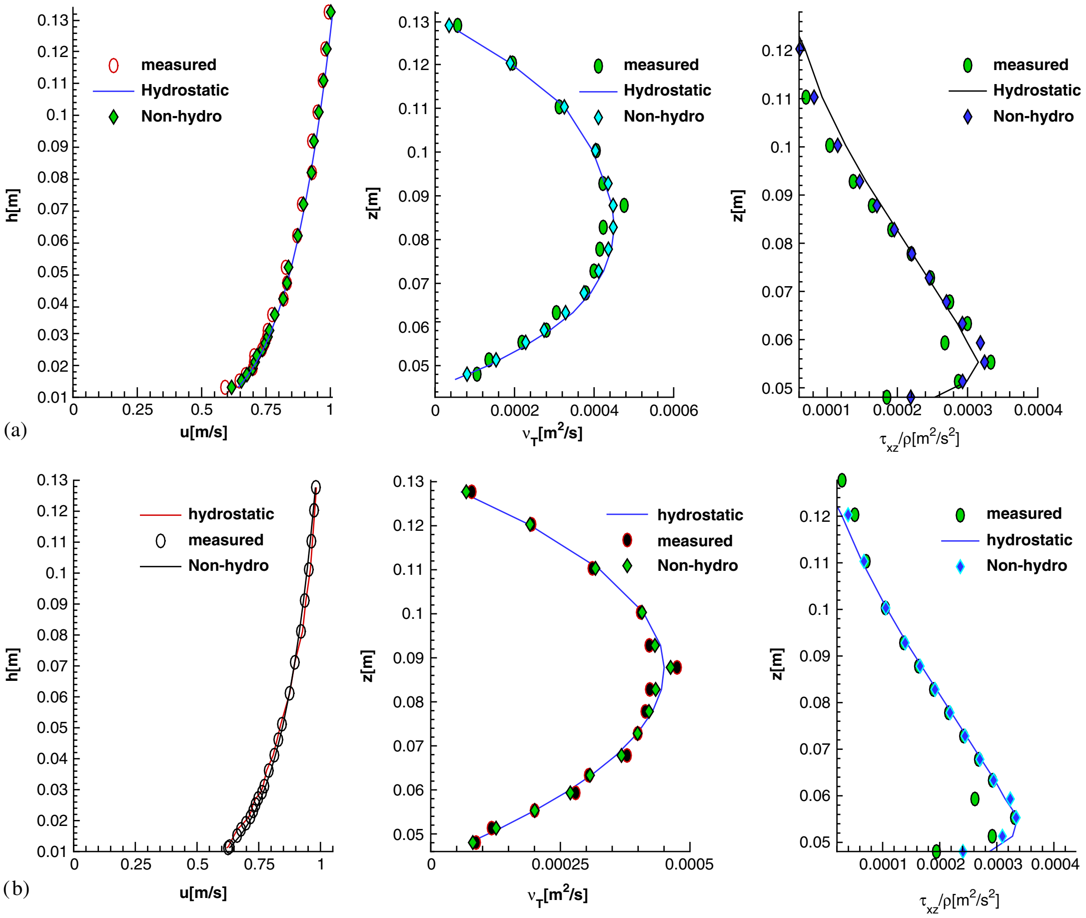

Figure 9. Comparison between computation hydrostatic solution (—), Non-hydrostatic solution (◇) and experiments (○) at the sections: (a) $x = 10.78$[m]; and (b) $x = 14.08$[m].

viscosity and shear stress profiles of the well developed flow compares favourably with the experiments. The eddy viscosity goes to zero near the free-surface, increases with the depth with a maximum around the mid-depth, and decreases towards zero near the bed. Figure 10 shows the more accurate solutions with the non-hydrostatic pressure. Computations agree well with experiments for the kinetic energy, its rate of dissipation and shear stress at the selected sections.

4.4. *Sharp and curved open channel: discussions*

The channel layout and dimension is shown in Figure 11. The discharge is set to $Q = 0.089$ [m/s], the bed slope $S_0 = 0.000624$. The rough bed is characterized by an equivalent roughness height, $k_s = 0.0022$[m]. The flow depth at the outflow (downstream end of the flume) is

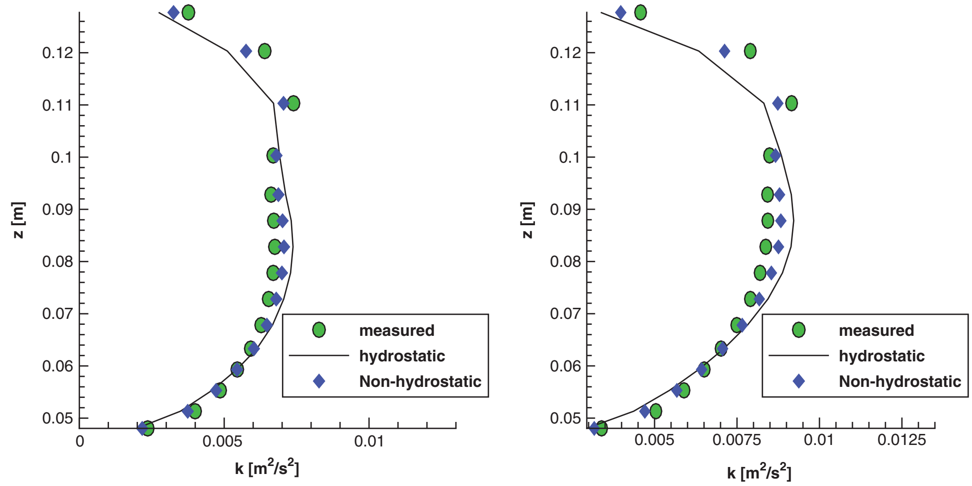

(a) x = 10.78[m] x = 14.08[m]

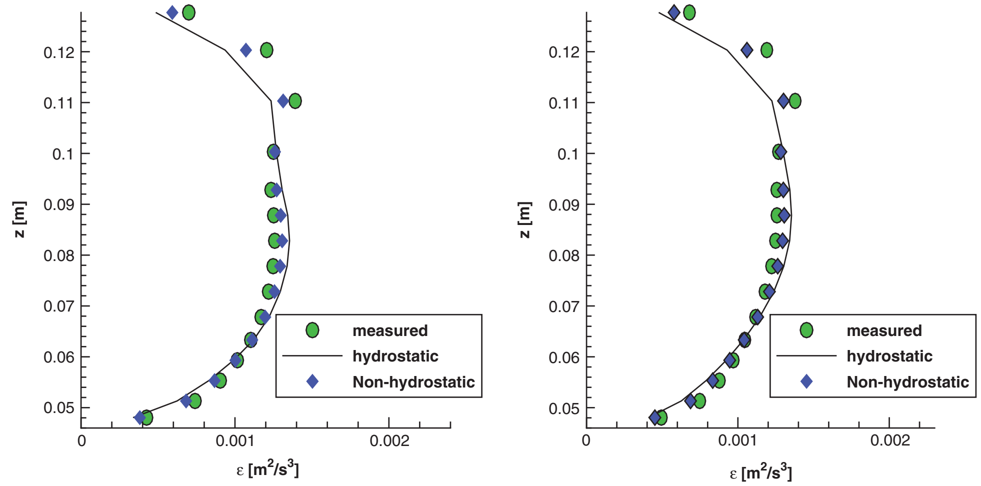

(b) x = 10.78[m] x = 14.08[m]

Figure 10. Comparison between computed and measured kinetic energy its dissipation at the selected sections: (a) comparison between numerical and experimental turbulent kinetic energy distributions at the selected sections; and (b) comparison between numerical and experimental turbulent dissipation of kinetic energy distributions at the selected sections.

0.159[m]. The experimental data are available for the flow case (see Reference [22]). The mean grid size of about $\Delta x = 0.05$[m], while the time-step size is set to $\Delta t = 0.1$ [s]. Computation is performed till the flow is well developed at $T = 1300$[s], using 60 layers, with the lowest layer thickness $\delta Z_b = 0.002$[m].

Computations were conducted with the hydrostatic pressure assumption for different cross-sections with the increasing curvature, to determine the conditions where the non-hydrostatic pressure component become significant.

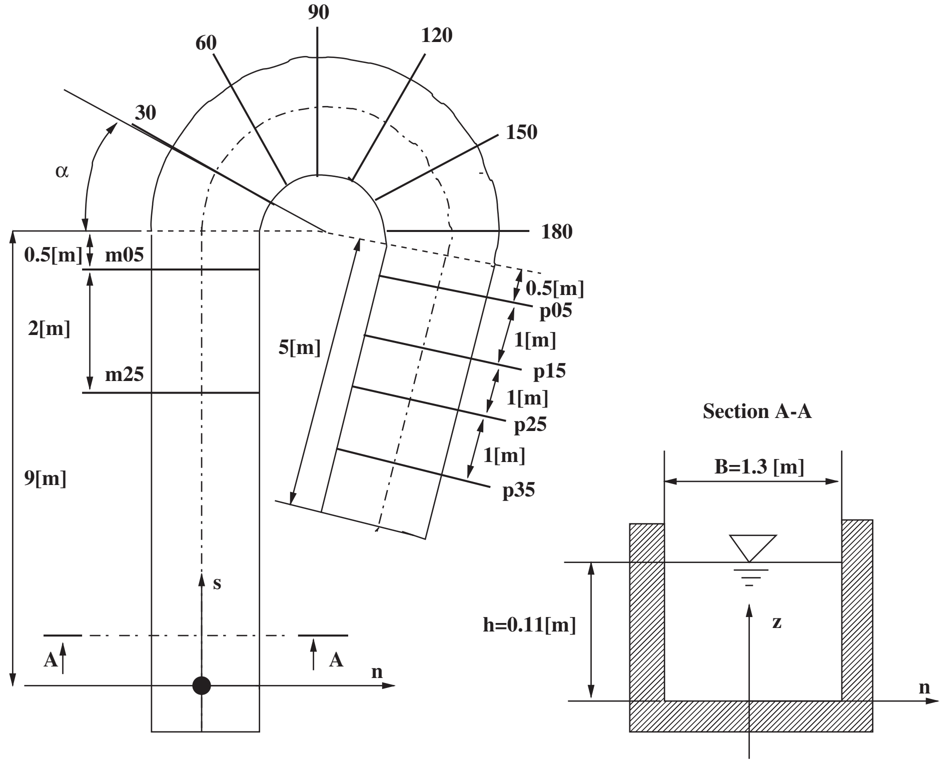

Figure 11. A 193° curved open channel.

Computations predict the gross flow features, while the water surface profile is under-estimated at the out bank, and over-estimated at the inner bank.

Figure 12 shows the cross-section at $\alpha = 120°$, where the conventional hydrostatic pressure is found to perform poorly. Here agreement with experiments is rather better with non-hydrostatic pressure, particularly with the increasing curvature. It seems likely that is due to the incorporation of free-surface movement as well as short waves. This suggest that, in curved channel flows, the pressure-driven secondary effects are important and the computation of free-surface must be more accurate to take into account the damping effects of free-surface.

In Figures 13 and 14, computations show only one secondary flow circulation rotating clockwise from inner bank to outer bank, i.e. the weak secondary currents are not predicted. The maximum under prediction in the secondary current for each vertical examined in this cross-section is ranged between 25 and 95% for non-hydrostatic solution, while the hydrostatic ones is ranged between 30 and 105%. These results suggest that this model can be considered to perform well (see also References [23, 24]). Figure 14 shows the centre of vortex position, that is located at about $z = 0.25$[m] for the hydrostatic solution, $z = 0.35$[m] for the non-hydrostatic solution while experiments is located at $z = 0.4$[m].

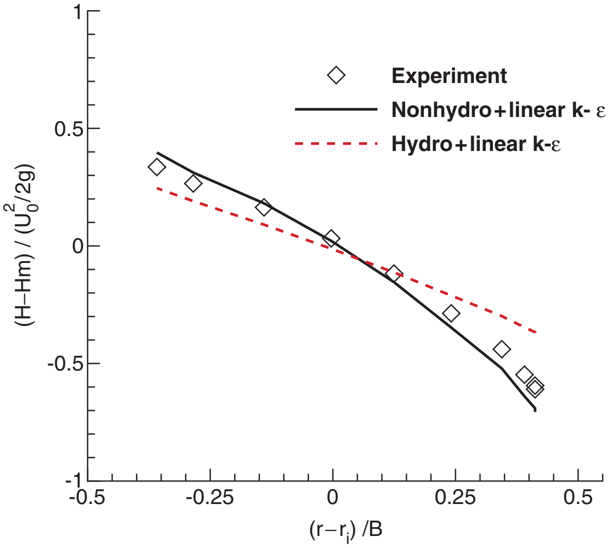

Figure 12. Experiments versus computed free-surface solutions at section $\alpha = 120°$ using linear k–ε turbulence model: experiment (◇); hydrostatic (dashed line); and non-hydrostatic (solid line).

Figure 15 shows the cross-wise longitudinal velocity component at the section $\alpha = 120°$, and the hydrostatic solution is over predicted, while the non-hydrostatic solution is more closed to the experiments. The computed maximum primary velocity is offset towards the channel centre relative to the outside of the bend, leading to the under prediction in secondary currents strength. This suggest that the turbulence-driven secondary effects are nonlinear. Whereas the anisotropic stress caused by walls and the junction region is not captured by the model, this leads to reduced momentum transfers towards the outer region of the bend with the consequence on the position of the maximum longitudinal velocity. Consequently, as shown by Gatski *et al.* [25], the related weaker turbulence-driven secondary motion cannot be reproduced by linear and isotropic eddy-viscosity turbulence models. However, the major flow features such as the presence and rotational sense of the major secondary currents are reproduced and agrees well with experiments. Moreover, the non-hydrostatic pressure influence is found to be more significant with the increasing curvature region. Therefore, although being more expensive, it become useful for such flows where its influence is thought to be significant. This suggest that the pressure-driven secondary currents is relatively important in the accurate description of the velocity field, while the use of anisotropic turbulence models is prerequisite to more accurate flow field prediction.

5. CONCLUSIONS

In the present work the validation of the 3D finite element solver for the Reynolds-averaged Navier–Stokes equations with the state-of-art k–ε turbulence closure is successfully conducted.

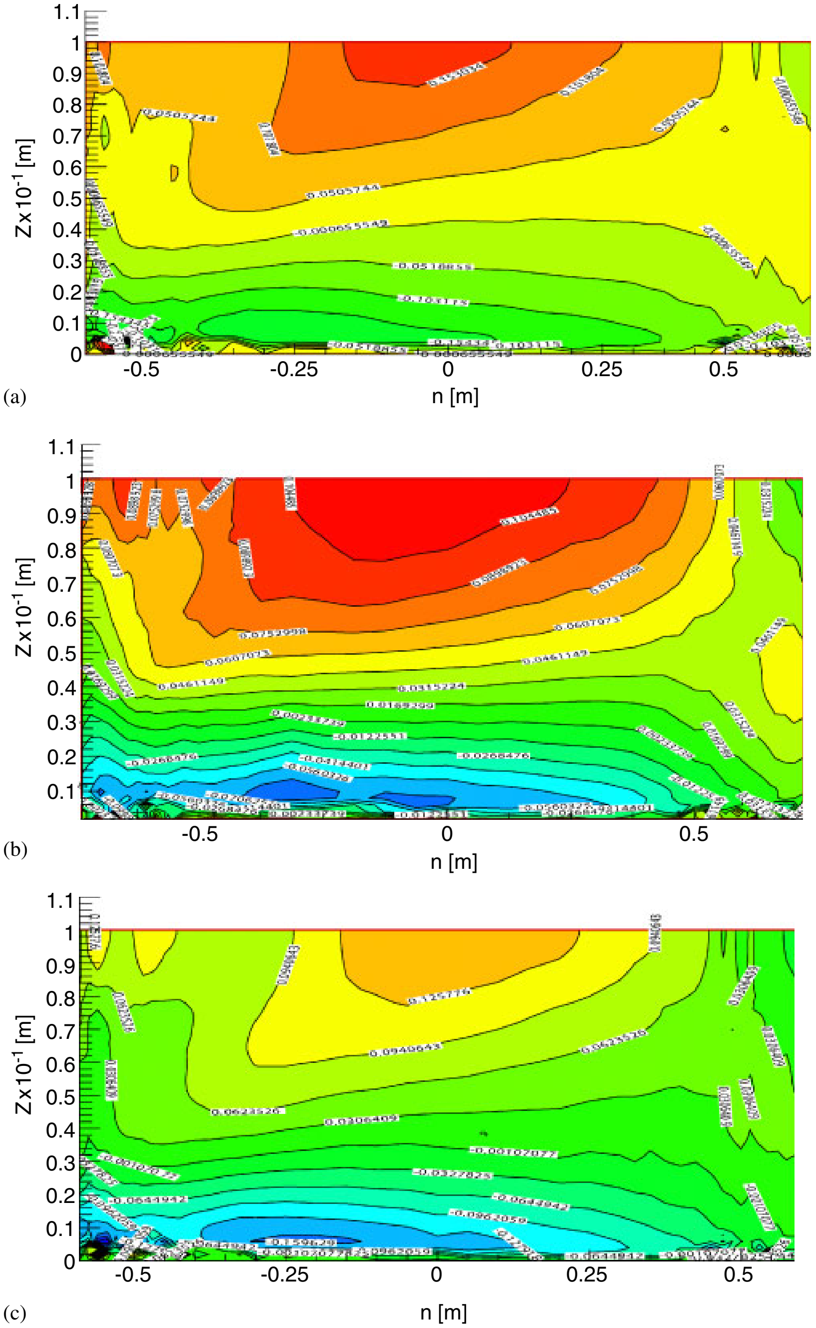

Figure 13. Experiments versus computed solutions of the transversal velocity component V_n of cross-stream at section $\alpha = 120^\circ$: (a) experiment; (b) hydrostatic; and (c) non-hydrostatic.

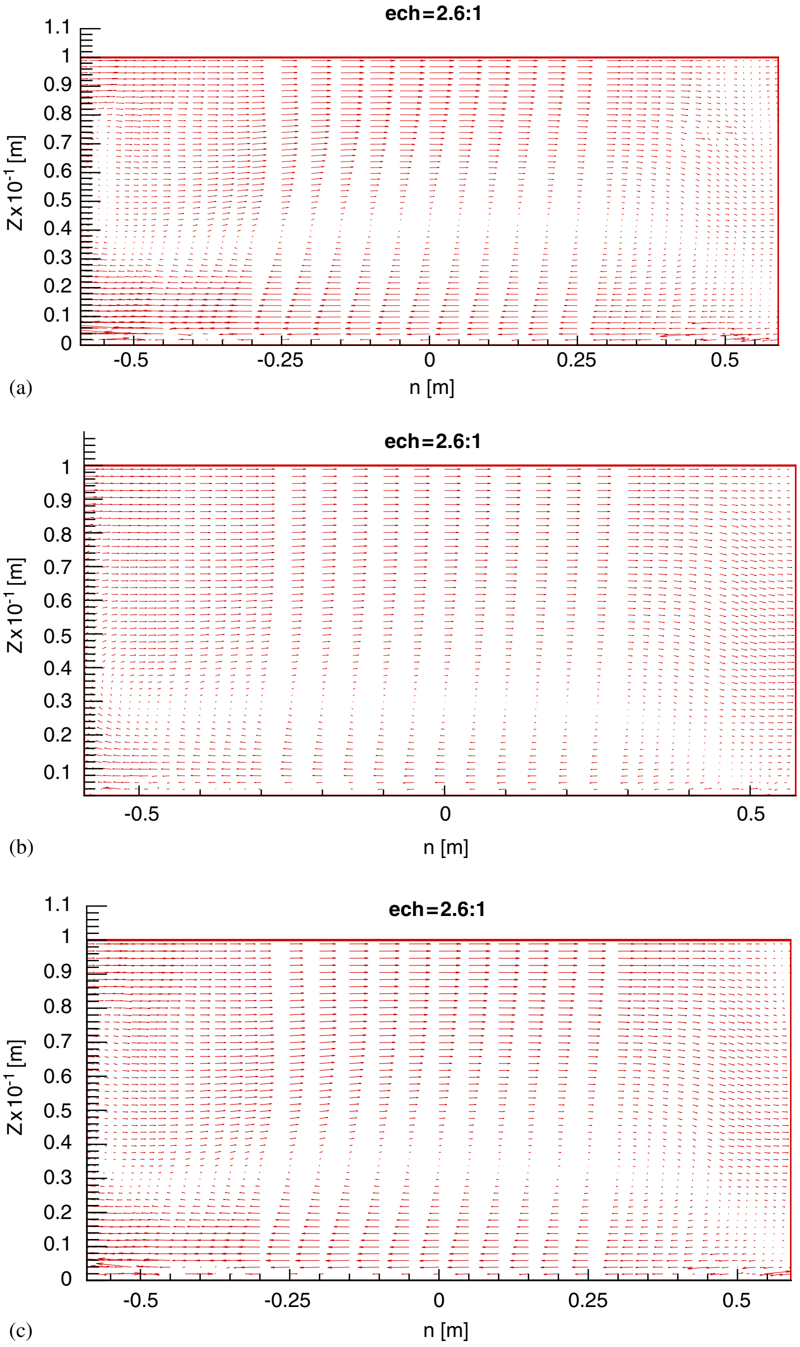

Figure 14. Experiments versus computed solutions of the cross-stream velocity vector at section $\alpha = 120°$: (a) experiment; (b) hydrostatic; and (c) non-hydrostatic.

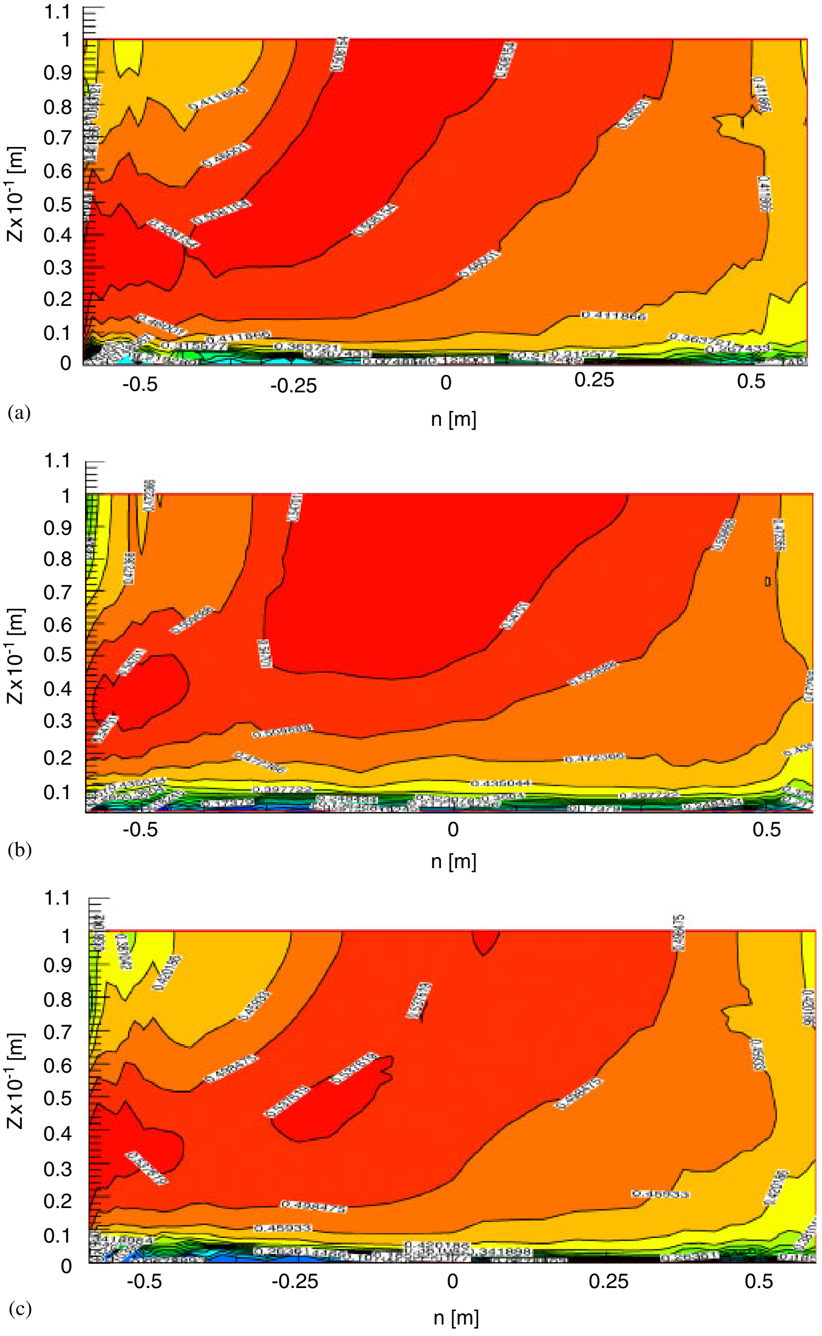

Figure 15. Experiments versus computed solutions of the stream-wise velocity component V_s of cross-stream at section $\alpha = 120°$: (a) experiment; (b) hydrostatic; and (c) non-hydrostatic.

The tests were performed in order to validate the model against well-known flows with the increasing complexity, using a high quality and high spatial resolution data set. The lower order Raviart–Thomas finite element is used for horizontal flux in the xy plane unstructured grid, together with a linear finite element scheme in the vertical direction. The model uses Lagrange–Galerkin approach to compute the convection terms, with the principal advantage that, owing to the Lagrangian (i.e. non-local) nature of the advection step, the CFL restriction is well performed. The model preserves the mass balance, the stability of the scheme and the positivity of k and ε. On the other hand, the unstructured grid offers possibility of greatly reduced grid generation effort for flows with complex geometry. Computations with and without non-hydrostatic are compared for the same trench to test the validity of the conventional hydrostatic pressure assumption. For the curved open channel, as expected, the linear k–ε model do not reproduces the weaker secondary current in the straight part of the channel. The non-hydrostatic pressure influence is found to be more significant with the increasing curvature region, and this suggest that the non-hydrostatic pressure (which is the computationally expensive part of the scheme) may be useful and well suited when a 3D description of flow field is needed or where its influence is thought to be significant. The model accuracy is found to be of order of $O(\Delta t, \Delta x^2)$, and the model predicts reasonably the complex major features and their consequences on the 3D flows. However, further study is needed to improve the general applicability of the model, and the next stage of this work will be focus on the non-uniform anisotropic turbulence-driven secondary motion.

ACKNOWLEDGEMENTS

The first author gratefully acknowledges the funding from the Swiss National Science Foundation through grant number 21-65095.01. Michel Deville, Alfio Quarteroni, Edie Miglio and Koen Blanckaert are acknowledged for their fruitful discussions.

REFERENCES

1. Johns B. The modeling of the free-surface flow over the topography. *Coastal Engineering* 1991; **15**:227–278.
2. Casulli V, Stelling G. Simulation of three-dimensional, non-hydrostatic free-surface flows for estuaries and coastal seas. *Proceedings of the International Conference on Estuarine and Coastal Modeling*. ASCE: New York, NY, U.S.A., 1996; 112.
3. Casulli V, Cheng RT. Semi-implicit finite difference methods for three-dimensional shallow water flow. *International Journal for Numerical Methods in Fluids* 1992; **15**:629–648.
4. Stansby PK, Zhou JG. Shallow-water flow solver with non-hydrostatic pressure: 2D vertical plane problems. *International Journal for Numerical Methods in Fluids* 1998; **28**:541–563.
5. Lai YG, Weber LJ, Patel VC. Three-dimensional model for hydraulic flow simulation. I: formulation and verification. *Journal of Hydraulic Engineering* (ASCE) 2003; **129**(3):196–205; 1090–1107.
6. Wu W, Rodi W, Wenka T. 3D numerical modeling of flow and sediment transport in open channels. *Journal of Hydraulic Engineering* (ASCE) 2000; **126**(1):4–15.
7. Olsen NRB. Three-dimensional CFD modeling of self-forming meandering channel. *Journal Hydraulic Engineering* (ASCE) 2003; **129**(5):366–372; 1090–1107.
8. Chao X, Jia Y, Wang SSY. Three-dimensional simulation of buoyant heat transfer in a curved open channel. *Proceedings of the International Conference on Advances in Hydro-science and -Engineering*, ICHE-vol. 6, NCCHE Mississipi, U.S.A., 2004; 18–19.
9. Leschziner MA, Rodi W. Calculation of strongly curved open channel flow. *Journal of Hydraulic Division* (ASCE) 1979; **103**(10):1297–1314.
10. Leupi C, Miglio E, Altinakar M, Quarteroni A, Deville M. QUASI-3D finite element shallow-water flow with k–ε turbulence model. *Proceedings of the International Conference on Advances in Hydro-science and -Engineering*, ICHE-vol. 6, Brisbane, Australia, 2004; 400–401 & On CD-ROM.
11. Mohammadi B, Pironneau O. *Analysis of k–ε Turbulence Model*. Wiley: Chichester, 1994.

12. Rodi W. Turbulence models and their application in hydraulics. *International Association for Hydraulic Research* (2nd edn), Delft, Netherlands.
13. Luyten PJ, Jones JE, Proctor R, Tabor A, Tett P, Wild-Allen K. COHERENS-A coupled hydrodynamical-ecological model for regional and shelf seas: user documentation. *MUMM Report*, Management Unit of the Mathematical Models of North Sea, 1999; 914.
14. Launder BE, Spalding DB. The numerical computation of turbulent flows. *Computer Methods in Applied Mechanics and Engineering* 1974; **3**:269–289.
15. Roland S. *Modélisation et simulation des Ecoulements turbulents*, Hermes, Paris, 1993.
16. Miglio E, Quarteroni A, Saleri F. Finite element approximation of Quasi-3D shallow water equations. *Computer Methods in Applied Mechanics and Engineering* 1999; **174**(34):355–369.
17. Raviart PA, Thomas JM. A mixed finite element method for 2nd order elliptic problems. In *Mathematical Aspects of Finite Element Methods*, Galliani I, Magenes E (eds), Lecture Notes in Mathematics. Springer: Berlin, 1997; 292–315.
18. Graf WH, Altinakar MS. *Hydraulique Fluviale, Presses Polytechniques et Universitaires Romandes*. CH-1015 Lausanne, Switzerland, 1993.
19. Istiarto I. Flow around a cylinder on a mobile channel bed. *Ph.D. Thesis No. 2368*, EPFL, Lausanne, Switzerland, 2001.
20. Michler C, Hulshoff SJ, van Brummelen EH, de Borst R. Monolithic approach to fluid-structure interaction. *Computers and Fluids* 2004; **33**:839–848.
21. Zhaosong Qu. Unsteady open-channel flow over a mobile bed. *Ph.D. Thesis No. 2688*, EPFL, Lausanne, Switzerland, 2002.
22. Blanckaert K. Flow and turbulence in sharp open-channel bends. *Ph.D. Thesis No. 2545*, EPFL, Lausanne, Switzerland, 2002.
23. Ye J, McCorquodale JA. Simulation of curved open channel flows by 3D hydrodynamic model. *Journal of Hydraulic Engineering* 1998; **124**(7):687–698.
24. Wilson CAME, Boxall JB, Guymen I, Olsen NRB. Validation of a three-dimensional numerical code in the simulation of pseudo-natural meandering flows. *Journal of Hydraulic Engineering* 2003; **129**(10):758–768.
25. Gatski TB, Hussaini MY, Lumley J. Simulation and modeling of turbulent flows. *ICASE/LaRC Series in Computational Science and Engineering*. Oxford University Press, Inc.: New York, U.S.A., 1996; 314.